

Strain Effects on the Oxidation of CO and HCOOH on Au–Pd Core–Shell Nanoparticles

Verónica Celorrio,[†] Paola M. Quaino,[‡] Elizabeth Santos,^{§,||} Jonathan Flórez-Montaña,[⊥] Jo J. L. Humphrey,[†] Olmedo Guillén-Villafuerte,[⊥] Daniela Plana,[†] María J. Lázaro,[@] Elena Pastor,^{*,†} and David J. Fermín^{*,†}

[†]School of Chemistry, University of Bristol, Cantocks Close, Bristol BS8 1TS, U.K.

[‡]Instituto de Química Aplicada del Litoral, IQAL (UNL-CONICET), PRELINE (FIQ-UNL), Santa Fe, Argentina

[§]Instituto de Física Enrique Gaviola (IFEG-CONICET), Facultad de Matemática, Astronomía y Física, FaMAF-UNC, Córdoba, Argentina

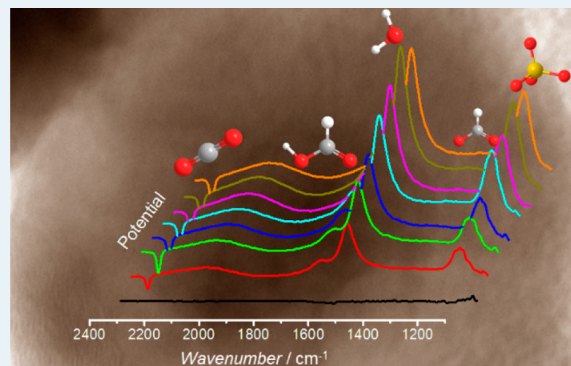
^{||}Institute of Theoretical Chemistry, Ulm University, Albert-Einstein-Allee 11, Ulm, Germany

[⊥]Departamento de Química e Instituto de Materiales y Nanotecnología, Universidad de La Laguna, Avda. Astrofísico Francisco Sánchez s/n, 38206 La Laguna, Tenerife, Spain

[@]Instituto de Carboquímica (CSIC), Miguel Luesma Castán 4, 50018 Zaragoza, Spain

Supporting Information

ABSTRACT: The mechanism of CO and HCOOH electrooxidation in an acidic solution on carbon-supported Au–Pd core–shell nanoparticles was investigated by differential electrochemical mass spectrometry and in situ Fourier transform infrared (FTIR) spectroscopy. Analysis performed in nanostructures with 1.3 ± 0.1 nm (CS1) and 9.9 ± 1.1 nm (CS10) Pd shells provides compelling evidence that the mechanism of adsorbed CO (CO_{ads}) oxidation is affected by structural and electronic effects introduced by the Au cores. In the case of CS10, a band associated with adsorbed OH species (OH_{ads}) is observed in the potential range of CO oxidation. This feature is not detected in the case of CS1, suggesting that the reaction follows an alternative mechanism involving COOH_{ads} species. The faradaic charge associated with CO_{ads} oxidation as well as the Stark slope measured from FTIR indicates that the overall affinity and orbital coupling of CO to Pd are weaker for CS1 shells. FTIR spectroscopy also revealed the presence of HCOO_{ads} intermediate species only in the case of CS1. This observation allowed us to conclude that the higher activity of CS10 toward this reaction is due to a fast HCOO_{ads} oxidation step, probably involving OH_{ads} to generate CO_2 . Density functional theory calculations are used to estimate the contributions of the so-called ligand and strain effects on the local density of states of the Pd d-band. The calculations strongly suggest that the key parameter contributing to the change in mechanism is the effective lattice strain.



KEYWORDS: formic acid, Au–Pd core–shells, DEMS, in situ FTIR, strain effect

INTRODUCTION

The catalytic activity of bimetallic structures can be significantly different from those of the individual components and can be tuned through the controlled growth of thin films on foreign supports.^{1,2} The reactivity of this type of system can be rationalized in terms of electronic and geometric (so-called strain) effects, which can alter the position of the d-band center.^{3,4} Pd overlayers on Au substrates have received a significant amount of attention for a variety of catalytic reactions, particularly in the context of the hydrogen evolution–oxidation reactions and formic acid oxidation, where it has been shown that the underlying Au substrate can alter the electrocatalytic activity of the Pd layers.^{5–11} The

generation of complex Pd-based nanostructures has also provided a rich variety of structures and compositions with interesting catalytic properties.^{12–15}

A strong dependence on the Au substrate structure has been experimentally demonstrated for the oxidation of adsorbed CO (CO_{ads}) on Pd overlayers.^{16,17} Density functional theory (DFT) calculations concluded that the CO_{ads} binding energy at pseudomorphic Pd overlayers on Au (111) surfaces goes through a maximal value for two overlayers,¹⁸ although it is not

Received: November 14, 2016

Revised: December 29, 2016

Published: January 17, 2017

clear how the computed strain of the relaxation mechanism compares with experimental values. The effective strain of Pd nanoshells on Au cores in the range of 1–10 nm can be described by the generation of edge dislocation with Burgers vectors of $1/2\langle 110 \rangle$ in the (111) plane.^{19,20} The Pd strain relaxation manifests as an increase in the charge associated with the oxidation of CO_{ads} , corrected by changes in the mean particle surface roughness.^{21–24}

The oxidation of HCOOH at Pd surfaces, contrary to the case of Pt, is commonly associated with the so-called direct mechanism in which no CO_{ads} intermediate is generated.^{21,22,25,26} It is proposed that the reaction rate is controlled by the oxidation of adsorbed formate (HCOO_{ads}) intermediates.^{25,27} Although the catalytic activity of HCOOH has been investigated as a function of the Pd content, the rationale for the experimental trends has not been clarified.

In this paper, the electrooxidation of CO_{ads} and HCOOH on Au–Pd core–shell nanoparticles, supported on Vulcan XC-72R, is studied by in situ Fourier transform infrared (FTIR) spectroscopy and differential electrochemical mass spectrometry (DEMS). The experimental data provide conclusive evidence that the surface binding of key intermediates is strongly affected by the Pd thickness. In particular, we show that CO_{ads} oxidation at CS10 particles undergoes a reaction with adsorbed OH (OH_{ads}) species, while no evidence of this intermediate was obtained in the case of CS1. CO Stark slopes obtained from FTIR spectra also show a significantly weaker orbital interaction with strained Pd shells. The Au-like features characterizing CS1 are further demonstrated by the detection of HCOO_{ads} intermediate species during the oxidation of HCOOH , an intermediate not observed in the case of CS10. We further rationalize the contrast in electrocatalytic activity by employing DFT calculations for model structures, assessing the role of ligand and strain (geometric) effects. Analysis of the Pd d-band local density of states strongly suggests that the contrast in electrocatalytic properties is primarily linked to strain in the Pd lattice.

RESULTS AND DISCUSSION

Characteristic transmission electron microscopy (TEM) images of 20 nm Au nanoparticles coated with 1.3 ± 0.1 nm (CS1) and 9.9 ± 1.1 nm (CS10) thick layers of Pd are illustrated in Figure 1. High-resolution imaging of the core–shell boundary shows lattice fringes extending from the Au core into the thin Pd layer in CS1 (Figure 1a), consistent with “quasi” epitaxial growth. Figure 1b shows a narrow size distribution, which is preserved upon dispersion over the carbon support (Figure 1c). Figure 1d shows high-resolution TEM images of a CS10 particle in which the contrast between the Pd shell and the Au core is visible under bright field mode. The dark field image in Figure 1e does provide a stronger contrast between the 10 nm Pd shell and the Au core, while Figure 1f also demonstrates a good dispersion of the particles once deposited onto the carbon support. EDX line-scan analysis in Figure S1 further confirms the core–shell configuration of these nanostructures, which is consistent with the low-temperature method used for depositing the Pd layer onto the Au cores.^{20–22,28} Indeed, previous electron diffraction studies performed on particles obtained by this method also reveal diffraction spots associated with the Au and Pd lattices, which allowed the effective strain of the shell to be estimated.^{19,20} The mean shell thickness was estimated as the difference between the average diameter of the core–shell and core nanoparticles based on the statistics of >200 particles from

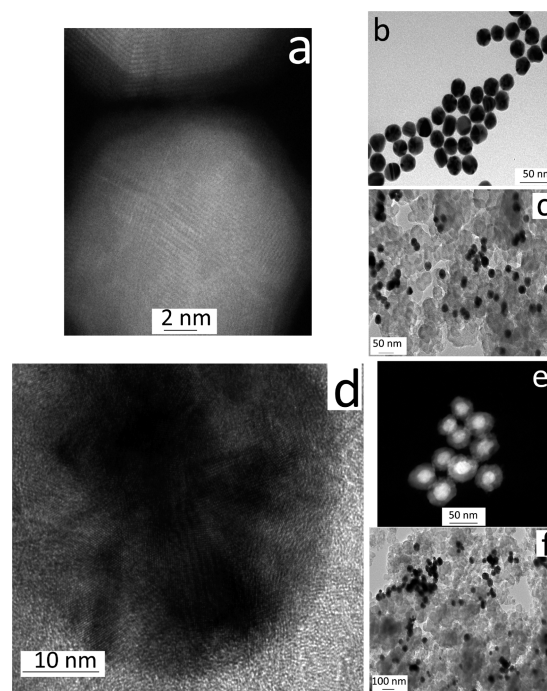


Figure 1. High-resolution TEM images of (a and b) CS1 and (d and e) CS10 samples demonstrating the core–shell nature of the nanostructures and size dispersion. TEM images of (c) CS1 and (f) CS10 samples showing a good dispersion of the metallic nanoparticles in the carbon support.

each composition (Table S1). The mean shell thickness correlates well with analysis of individual particles employing STEM–EDX line-scan analysis (Figure S1). Consequently, the structure–activity relationships described below are based on the most representative particle dimensions, as opposed to a small selection of particles imaged by electron microscopy.

Figure 2 shows typical cyclic voltammograms for the oxidation of a monolayer of adsorbed CO on CS1 and CS10 catalysts in 0.5 M H_2SO_4 . The data are magnified in the potential range in which CO oxidation occurs, while voltammograms across the whole potential range can be found in Figure S2. Both catalysts exhibit a CO_{ads} oxidation peak at around 0.9 V, although CS10 is characterized by a significantly sharper response. CS10 also exhibits a prepeak that has been assigned to the oxidation of CO_{ads} at defect sites, which is consistent with the fact that these particles exhibit a degree of surface roughness.^{16,21} The dashed lines in both voltammograms correspond to the responses recorded during the second potential cycle. The second cycle corresponds to a CO-free Pd surface; thus, the difference in faradaic charges recorded in the first and second forward sweep is effectively proportional to the population of adsorbed CO. Calculations of effective surface areas are nontrivial, which we have tackled by quantifying several independent surface sensitive probes, including hydrogen adsorption, hydrogen absorption, oxide reduction, and oxidation of adsorbed CO.^{20,21} This multi-parameter approach allows a self-consistent analysis of the effective surface area regardless of uncertainties in particle loading, the amount of catalyst layer deposited on the electrode, the particle size, and the mean nanoparticle surface roughness. For example, the charge associated with CO_{ads} oxidation at CS10 particles (0.31 mC cm^{-2}) is very close to the values reported for bulk Pd, while the corresponding charge for CS1

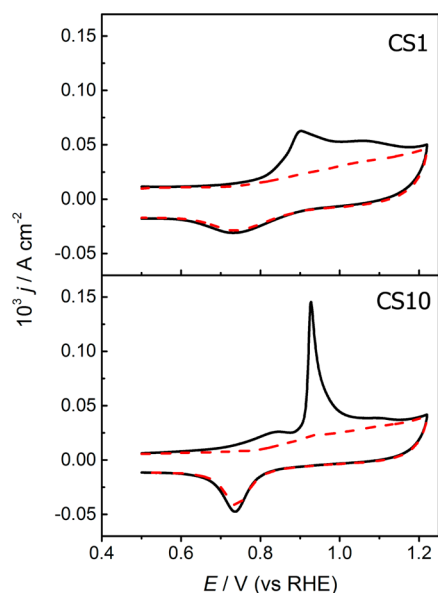


Figure 2. Cyclic voltammograms of the adsorbed CO oxidation at CS1 and CS10 catalysts in 0.5 M H_2SO_4 , recorded at 0.020 V s^{-1} . The electrode potential was held at 0.20 V vs a reversible hydrogen electrode. After adsorption, and prior to the voltammograms being recorded, excess CO was displaced from the solution by purging high-purity Ar. The black solid line corresponds to the first cycle (starting with the maximal CO coverage), while the second cycle is displayed as a red dotted line (CO-free surface).

(0.16 mC cm^{-2}) approaches values observed at pseudomorphic Pd monolayers on Au(111) surfaces.²¹ It should be mentioned that comparisons with pure Pd nanoparticles on carbon supports are not straightforward because of the influence of a variety of parameters such as particle size and functional groups on the carbon support.^{21,28}

The oxidation of CO_{ads} is commonly associated with a surface bimolecular reaction involving adsorbed OH species (OH_{ads}), which is not linked to any clear voltammetric feature. Consequently, the shape of the voltammogram does not provide direct evidence of the oxidation mechanism or the CO binding energy. We shall address some of these issues employing in situ FTIR.

Figure 3 shows FTIR spectra obtained in the range of 0.2–1.2 V versus a reversible hydrogen electrode (RHE) in the presence of an adsorbed CO monolayer at CS1 (a and c) and CS10 (b and d). The spectrum at 0.20 V (E_{ref}), corresponding to the maximal CO coverage, was used as a reference. The emergence of positive bands at a given potential (E) indicates a decrease in the population of species responsible for the IR absorption with respect to the population at E_{ref} . Initially, a bipolar signal is observed in both samples at $1970\text{--}1920 \text{ cm}^{-1}$, which is ascribed to bridge-adsorbed CO (CO_{B}).²⁹ As the potential is increased from 0.90 to 1.2 V, this band becomes positive, indicating that CO_{ads} is being oxidized. The negative band at 2343 cm^{-1} corresponds to CO_2 .²⁹ The onset potential for the CO_2 band is 0.50 V for CS10 and 0.70 V for CS1. This result indicates that the onset potential for CO_{ads} oxidation is more negative in the case of CS10.

A close inspection of the spectral range between 3800 and 3600 cm^{-1} (Figure 3c,d) shows the development of a negative band at approximately 3700 cm^{-1} in the case of CS10. This band is associated with OH_{ads} stretching,^{30,31} the population of which decreases as the applied potential increases. The fact that

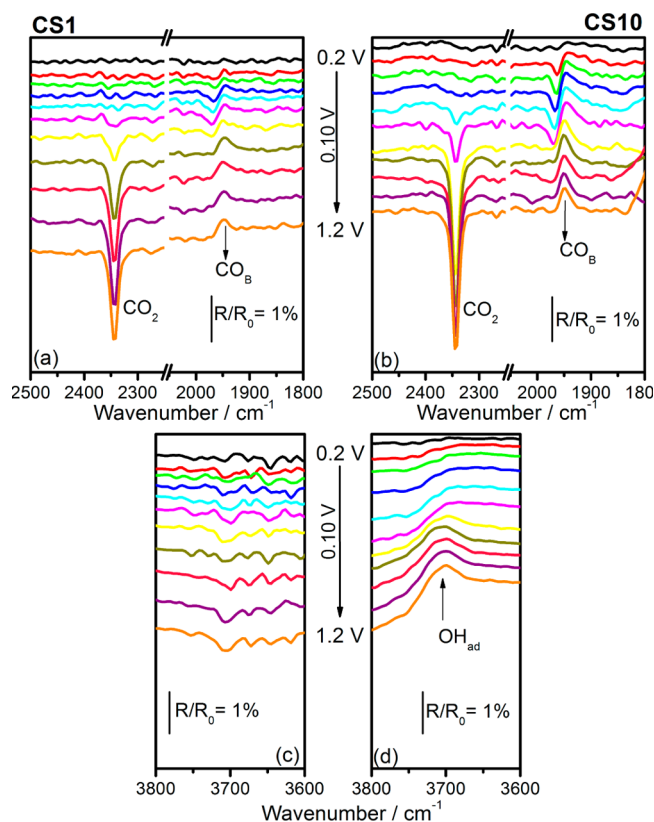
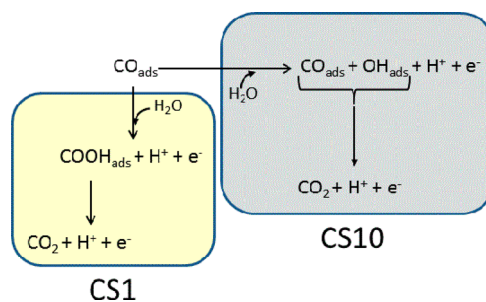


Figure 3. In situ FTIR spectra of the adsorbed CO oxidation on (a and c) CS1 and (b and d) CS10 in 0.5 M H_2SO_4 . The potential was increased from 0.20 V (reference potential) to 1.20 V. Each trace represents the average of 128 spectra at 8 cm^{-1} resolution.

the 3700 cm^{-1} feature is absent in the case of CS1 has very interesting implications for the mechanism of adsorbed CO oxidation as summarized in Scheme 1. In the case of CS10,

Scheme 1. Reaction Pathways for Adsorbed CO Oxidation on CS1 and CS10 Nanostructures



CO_{ads} electrooxidation is promoted by OH_{ads} species generated from water molecules interacting with the Pd surface to generate CO_2 , a process previously established for bulk Pd.³² In contrast, this reaction undergoes an alternative pathway at the surface of CS1 particles, most likely involving adsorbed carboxylate species (COOH_{ads}) formed by a direct reaction between CO_{ads} and water. This adsorbate is not stable and rapidly decomposes to CO_2 , as proposed in previous studies.^{27,33} The short lifetime and low coverage of this intermediate could justify the fact that it cannot be detected spectroscopically.²⁷

Figure 4 illustrates the integral of the band intensities assigned to CO_B and CO_2 at each electrode potential

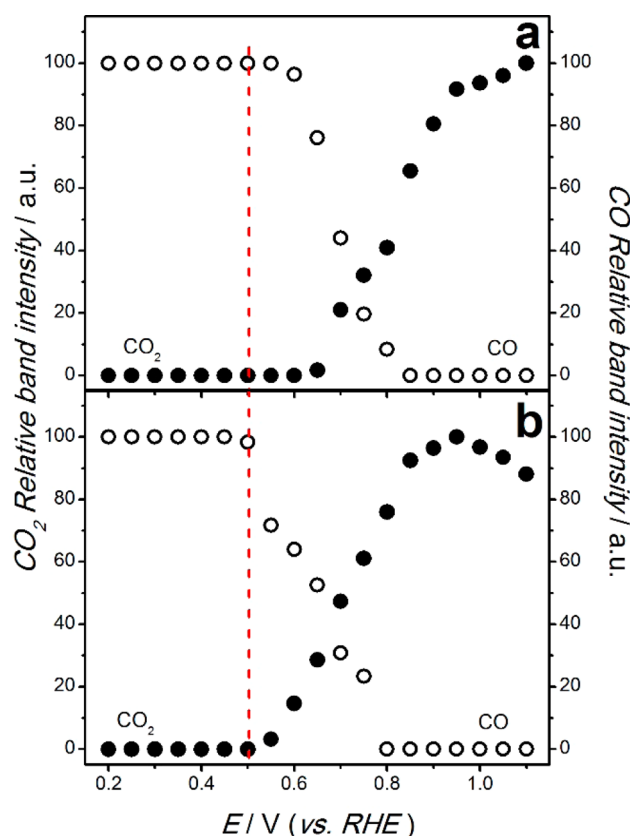


Figure 4. Potential dependence of the integrated band intensity for CO_B (O) and CO_2 (●) obtained from CO_ads oxidation spectra of (a) CS1 and (b) CS10. The integrated responses were normalized by the maximal value to account for small changes (<10%) in reflectivity from the various samples.

employing the method developed by Iwasita and Nart.²⁹ Integration of the CO_2 band was easily performed for the spectra presented in Figure 3. However, it was not possible to directly integrate the CO_B band because of its bipolar character. Consequently, the reference spectrum was changed to one at which no adsorbed CO_B was present on the surface, to obtain monopolar bands. In this case, the spectrum acquired at 1.10 V was taken as a reference for the calculation of the FTIR spectra and the whole series was replotted as shown in Figure S3. For both electrodes, the CO_B band intensity remains constant in the potential region prior to the onset of CO_B oxidation and decreases as the formation of CO_2 occurs. The data show that the onset of CO_2 formation is approximately 150 mV more negative at CS10 than at CS1.

The potential dependence of the CO_B band center (obtained from the spectra in Figure S3) is displayed in Figure 5. The upshift of the band center with increasing applied potentials can be linked to (i) metal-induced changes in the population of the CO antibonding orbital (back-bonding effect), (ii) perturbations of the vibration frequency due to the static double-layer electric field (Stark effect), and (iii) lateral interactions between adsorbed molecules.^{34,35} Firstly, it can be observed that the CO_ads stretching frequency at 0.20 V is similar for both catalysts (1951 and 1948 cm^{-1} for CS1 and CS10, respectively). However, there are significant differences with regard to the

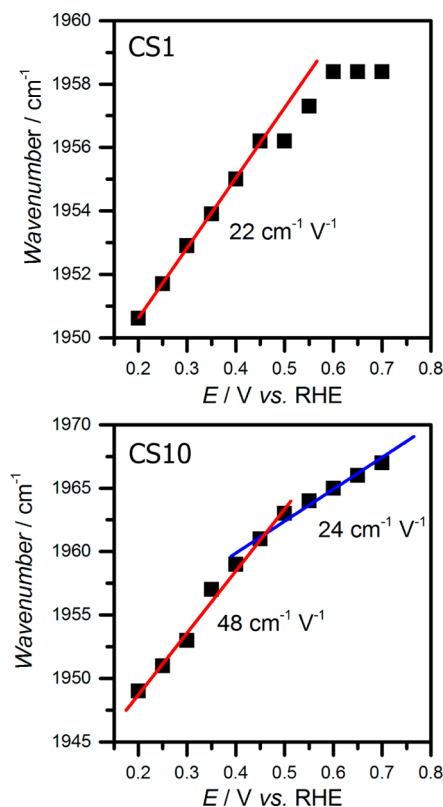


Figure 5. Potential dependence of the C–O stretch wavenumber adsorbed on CS1 and CS10.

change in the wavenumber with potential (i.e., dv/dE , commonly known as the Stark slope). It is observed that between 0.20 and 0.45 V the Stark slope for CS1 is 22 $\text{cm}^{-1} \text{V}^{-1}$ while CS10 shows a value of 48 $\text{cm}^{-1} \text{V}^{-1}$. The Stark slope of CS10 is close to the values reported for bulk Pd crystals and Pd adlayers at Pt surfaces,^{36–38} suggesting strong binding of CO to the relaxed Pd shell. On the other hand, the shallower Stark slope in CS1 reveals a weaker back-donating effect and, consequently, weaker CO bonding. This trend is consistent with the view that strained Pd shells adopt catalytic behavior similar to that of the Au core, which is characterized by weak CO bonding in acidic media.^{33,39,40} It is interesting to see a decrease in the Stark slope of CS10 to values close to CS1 in the potential range of CO_ads oxidation (between 0.45 and 0.70 V), suggesting a weakening of CO binding. This observation is yet to be fully rationalized, although it suggests a nontrivial link between CO coverage and binding strength.

Figure 6 shows the cyclic voltammograms (black line) and the simultaneously recorded mass spectrometric cyclic voltammograms (MSCVs, red lines) for m/z 44 (corresponding to CO_2) for CS1 and CS10 in 0.1 M HCOOH and 0.5 M H_2SO_4 . In both cases, the CO_2 mass signals follow the corresponding voltammetric profile of formic acid oxidation, albeit with a slight offset because of the lag time between the formation and detection of CO_2 . Via calculation of the current efficiency (ϵ^{CO_2}) as described in the Supporting Information, values of approximately 100% were estimated, confirming CO_2 as the only product in formic acid oxidation. The differences between the currents in the CVs and the Faradaic currents calculated from the MSCVs could be due to the contribution of double-layer charging and OH adsorption–desorption processes to the current in the CVs.⁴¹

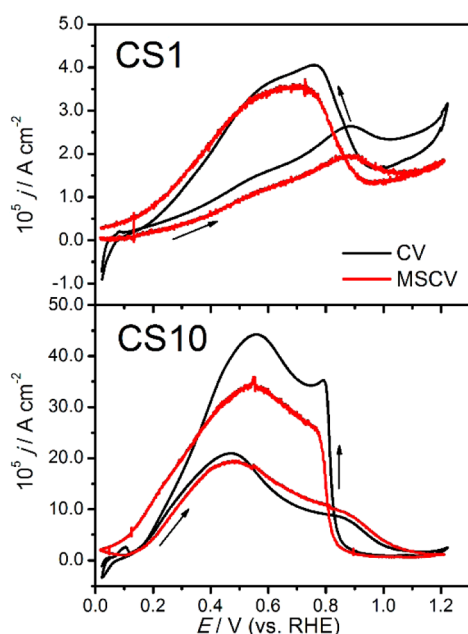


Figure 6. Faradaic currents associated with the oxidation of HCOOH obtained from CV (black) and MSCV (red). The MSCV signal was calculated from m/z 44 (CO_2). The electrolyte solution contained 0.1 M HCOOH and 0.5 M H_2SO_4 . The electrode potential was scanned at 1 mV s^{-1} .

Figure 7 shows the FTIR spectra recorded during formic acid electrooxidation as the potential is increased from 0.05 V (reference potential) to 1.20 V. The spectra exhibit three positive bands around 1200, 1620, and 1700 cm^{-1} , which correspond to bisulfate/sulfate anions, water bending, and carbonyl vibration from HCOOH, respectively.^{29,39,41} The negative band located at 2343 cm^{-1} is attributed to the formation of CO_2 during oxidation. The strong response from water (1620 cm^{-1}) introduces some complexity into the spectral analysis around this frequency range. However, it is clear that the sharp features associated with CO_{ads} are absent in the spectral responses at CS1 and CS10, indicating that oxidation of HCOOH to CO_2 proceeds through the direct pathway.^{21,25,42} A negative band at 1290 cm^{-1} assigned to HCOO_{ads} is observed as the potential is made more positive in the case of CS1 (Figure 7c), but not on the CS10 catalyst (Figure 7d). This observation strongly suggests that the lifetime of HCOO_{ads} intermediates is significantly shorter on CS10 than on CS1.

As in the case of CO, the contrast in reactivity (current) and the presence of HCOO_{ads} as an intermediate species in CS1 strongly suggest a Au-like behavior at the strained Pd shells, promoting a different pathway as summarized in Scheme 2. Indeed, an in situ surface-enhanced Raman spectroscopy (SERS) study by Beltramo and co-workers identified HCOO_{ads} as the intermediate species in the oxidation of HCOOH at Au electrodes, in addition to little dependence of the oxidation current on the HCOOH concentration, concluding that HCOO_{ads} oxidation is the rate-determining step.⁴⁰ At platinum electrodes, HCOO_{ads} has previously been reported to act as a site-blocking spectator in the oxidation of formic acid.⁴³ Consequently, the weaker activity of CS1 toward the HCOOH can be linked to the formation of stable HCOO_{ads} . On the other hand, the fast oxidation of HCOO_{ads} at CS10 could be linked to either a weaker HCOO_{ads} binding to the

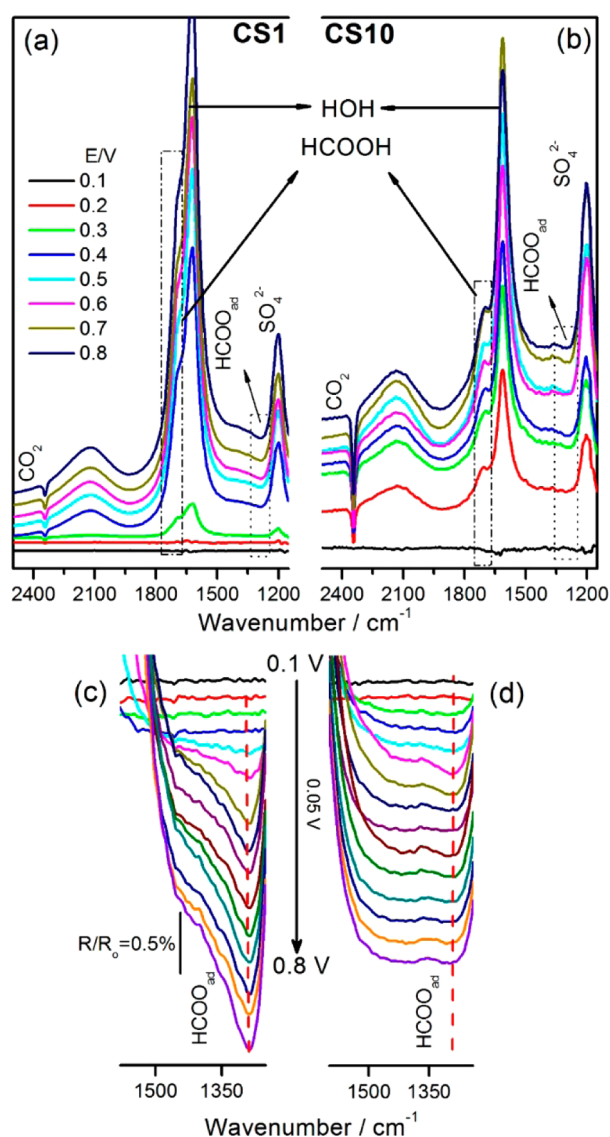
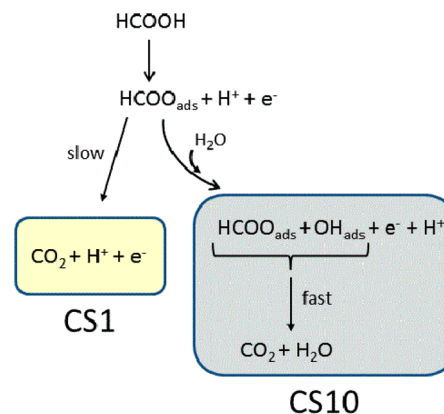


Figure 7. In situ FTIR spectra recorded during formic acid electrooxidation at (a and c) CS1 and (b and d) CS10 catalysts. The electrolyte solution contained 0.1 M HCOOH and 0.5 M H_2SO_4 . The potential was changed from 0.1 V (reference potential) to 0.8 V vs a RHE in steps of 0.05 V, averaging 128 spectra at a resolution of 8 cm^{-1} .

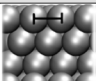
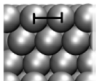
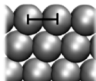
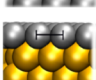
Scheme 2. Proposed HCOOH Oxidation Pathways of CS1 and CS10 Nanoparticles



relaxed Pd shell or a fast bimolecular reaction involving OH_{ads} species (as shown in the spectral features in Figure 3). Given that we have no direct evidence of strain-dependent HCOO_{ads} binding strength, we postulate the bimolecular reaction pathway (Scheme 2) as the most likely process promoting the fast HCOOH oxidation at CS10 particles.

The contrast in CO affinity and mechanism for formic acid oxidation provides a clear indication of changes in the electronic structure of the Pd shells as a function of thickness. However, whether these changes are exclusively related to strain or whether ligand effects do play a role it is yet to be clarified. To address this point, we have performed DFT calculations to estimate the local density of d states (LDOS), employing the effective strain relaxation parameters observed experimentally as shown in Table 1. Details of the methods of

Table 1. Pd d-Band Center (ϵ_{d}) as a Function of the Mean Pd Shell Thickness and Effective Lattice Constant (a_0)

	Shell Thickness (nm) ^a	Model	a_0 (Å) ^b	ϵ_{d} (eV)
CS10	9.9		3.9159	-2.0066
CS5	5.1		3.9499	-1.9211
CS1 (artificial)	1.3		4.027	-1.7424
CS1	1.3		4.027	-1.7972

^aShell thickness of CS5 taken from ref 19. ^bData obtained from selected area electron diffraction reported in ref 19.

calculation can be found in Section 1 of the Supporting Information. The strategy implemented in these calculations is inspired by the work by Quaino et al.,⁴⁴ contrasting the electronic structure of the CS1 Pd shells in the presence and absence (denoted as artificial structure) of the Au core. To reduce computational cost, CS1 is modeled as a Pd monolayer (as opposed to the three atomic layers corresponding to a mean thickness of 1.3 nm), although the 3.4% tensile strain observed experimentally was maintained.²⁰ We have also computed the case of Pd shells with a mean thickness of 5.1 nm (CS5), representing the case of a partially strained lattice. We explicitly ignore ligand effects in the case CS5 and CS10, given that these structures involve >13 Pd atomic layers. This approximation is supported by previous DFT studies.⁴⁴

The local densities of states (LDOS) projected on the d-band for the various structures investigated are shown in Figure 8. The d-band shows an upward shift with a decreasing shell thickness, with a slight peak narrowing. Introducing ligand effects in the case of CS1 generates further narrowing of the d-band features and an ~50 meV downward shift of the d-band center with respect to CS1 artificial. However, the ligand effects introduced by the Au states are somewhat overestimated on the basis of the fact that the Pd dimensionality is reduced to a monolayer. Consequently, the calculated contributions from ligand effects are most likely to be negligible in comparison

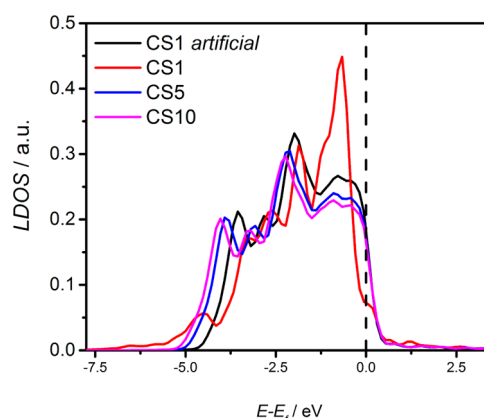


Figure 8. Density of states projected on the d-band for CS10, CS5, CS1, and CS1 artificial (ignoring ligand effects).

with the estimated 200 meV shift introduced by the strain effects.

Finally, it is interesting to place these findings in the context of our previous studies of CO_2 reduction.^{23,45} The experimental evidence shows that the primary product in CS1 particles is CO, while CS10 will produce formate at low overpotentials. The studies presented here show that an effective tensile strain of 3.5% characteristic of CS1²⁰ weakens binding of CO to the Pd layer, which is consistent with CO being the main product of CO_2 reduction. On the other hand, fully relaxed Pd CS10 leads to a strong CO binding that promotes the formation of not only HCOO^- but also methane and ethane.

CONCLUSIONS

FTIR and DEMS studies of carbon-supported Pd–Au core–shell nanoparticles reveal significant changes in the reactivity and mechanism of CO_{ads} and HCOOH oxidation reactions as a function of Pd strain. Investigations were focused on Pd shells featuring thicknesses of 1.3 ± 0.1 nm (CS1) and 9.9 ± 1.1 nm (CS10), which are characterized by tensile strain values of 3.5 and 1%, respectively.²⁰ FTIR studies show evidence of the formation of OH_{ads} at CS10, which reacts with adsorbed CO through a bimolecular surface reaction. No OH_{ads} intermediates are detected in the case of CS1, suggesting that the reaction follows a different path involving the formation of the carboxylic species COOH_{ads} as a short-lived intermediate. Furthermore, a significantly shallower Stark slope was observed in the case of CS1, suggesting CO orbital coupling with the strained Pd layer.

DEMS and FTIR studies showed that formic acid oxidation is characterized by a 100% conversion to CO_2 in the absence of CO intermediates at both catalysts, confirming the so-called “direct mechanism”.^{21,25,42} However, FTIR responses show the presence of HCOO_{ads} only in the case of CS1. This behavior suggests that HCOO_{ads} has a very short lifetime at CS10, probably because of the presence of OH_{ads} which can promote the fast oxidation to CO_2 . The stronger interaction between HCOO_{ads} and CS1 further confirms the Au-like behavior of the strain Pd shells, which manifests itself by a lower activity toward HCOOH oxidation. DFT calculations showed that the center of the d-band is upshifted by >0.26 eV with an increase in the lattice strain of the Pd shell from 1.0% (CS10) to 3.5% (CS1). The d-band shift is slightly less pronounced (by no more than 50 meV) if we include electronic effects arising from the Au core, indicating that the variations in mechanism and activity

between CS1 and CS10 are mainly determined by strain effects. Finally, it should be mentioned that a direct link between the electronic structure of thin Pd layer and reaction pathways does require DFT calculations involving intermediate species and solvation effects, as recently illustrated by Schmickler and co-workers in relation to the oxygen reduction reaction.⁴⁶ Arce et al. have also shown that OH adsorption at Pt strongly influences the metal surface electronic structure, even at low coverages.⁴⁷ We conclude that, although a strong correlation between reaction pathways experimentally determined and the calculated strain effect on the Pd d-band center is demonstrated in this work, fundamental mechanistic insights remain to be fully rationalized.

■ EXPERIMENTAL SECTION

FTIR and Cyclic Voltammetry Measurements. Electrochemical experiments were performed in a three-electrode electrochemical cell connected to an Autolab PGSTAT302N instrument. A large-surface area carbon rod was used as a counter electrode, and a RHE in the supporting electrolyte was employed as a reference electrode. All potentials in the text are referenced to this electrode. The working electrode was prepared by ultrasonically dispersing 2 mg of the electrocatalysts in 0.5 mL of pure water (Millipore) and 15 μ L of Nafion. An aliquot of the dispersed suspension was drop-cast onto the top of the working electrode and dried at ambient temperature. The working electrode supports were glassy carbon electrodes for CO_{ads} oxidation (7.0 mm diameter) and a gold disk for Fourier transform infrared spectroscopy (10 mm diameter). The experiments were performed in a 0.5 M sulfuric acid (Merck p.a.) solution prepared with Milli-Q water (Millipore). Fourier transform infrared spectroscopy experiments were performed with a Bruker Vector 22 spectrometer equipped with a mercury cadmium telluride detector. A small glass flow cell with a CaF₂ prism at its bottom was used. FTIR spectra were acquired from the average of 128 scans, obtained with 8 cm⁻¹ resolution at selected potentials, by applying 0.05 V single-potential steps from a reference potential, in the positive direction. The reflectance ratio R/R_0 was calculated, where R and R_0 are the reflectance values measured at the sample and the reference potential, respectively. In this way, positive and negative bands represent the loss and gain of species at the sampling potential, respectively.

DEMS Setup. The gaseous and volatile species produced on the electroactive surface can be followed online by DEMS. The experiments were conducted in a three-electrode electrochemical cell made of Plexiglass, at room temperature and atmospheric pressure. The counter electrode was a large-surface area carbon rod, and the reference electrode was a RHE placed inside a Luggin capillary. The working electrode was fixed between a PTFE membrane (Scimat) and a glassy carbon rod, connected to a Au wire that served as the electrical contact. The experimental setup allows the simultaneous acquisition of mass spectrometric cyclic voltammograms (MSCVs) for selected m/z (mass to charge) ratios and conventional cyclic voltammograms (CVs). Details of the setup calibration are given in the Supporting Information and in previous publications.⁴⁸

Electrocatalysts were deposited onto gas diffusion electrodes (GDEs) that were 7 mm in diameter following previously established procedures.⁴⁹ Briefly, a microporous layer was prepared by mixing Vulcan XC-72R, ultrapure water, isopropanol (Merck, p.a.), and a PTFE dispersion (60 wt %, Dyneon) and painted onto one side of a carbon cloth until a

final loading of 0.8 mg cm⁻² was achieved. To fix this layer, the carbon cloth was treated at 280 °C for 0.5 h and at 350 °C for 0.5 h. Electrocatalyst inks were prepared by mixing the respective electrocatalysts with a Nafion dispersion (5 wt %, Sigma-Aldrich) and ultrapure water [1:5:10 (w/w)] and deposited onto the GDE. The final metal loading of the working electrodes was 0.7 mg of metal cm⁻².

■ ASSOCIATED CONTENT

Supporting Information

The Supporting Information is available free of charge on the ACS Publications website at DOI: 10.1021/acscatal.6b03237.

Experimental methods associated with synthesis, characterization, DEMS calibration, and DFT calculations; STEM–EDX mapping of CS1 and CS10; full CO_{ads} oxidation voltammograms and FTIR spectroelectrochemistry of CO_{ads} oxidation (PDF)

■ AUTHOR INFORMATION

Corresponding Authors

*E-mail: E.Pastor@ull.es.

*E-mail: David.Fermin@bristol.ac.uk.

ORCID

Verónica Celorrio: 0000-0002-2818-3844

David J. Fermin: 0000-0002-0376-5506

Notes

The authors declare no competing financial interest.

■ ACKNOWLEDGMENTS

V.C. gratefully acknowledges the UK National Academy for their support through the International Newton Fellowship program (NF120002). D.P. and D.J.F. gratefully acknowledge funding from EPSRC (EP/K007025/1). J.J.L.H. is grateful for the Ph.D. scholarship partly funded by Sasol UK and NERC. E.P. acknowledges financial support from the Ministry of Economy and Competitiveness through Project ENE2014-52158-C2-2-R. D.J.F. is also grateful for the Research Fellowship from the Institute of Advanced Studies of the University of Bristol. TEM studies were performed at the University of Bristol Chemistry Imaging Facility with equipment funded by UoB and EPSRC (EP/K035746/1 and EP/M028216/1). We are grateful to Prof. Jeremy Sloan (University of Warwick, Coventry, U.K.) and Dr. Christoph Mitterbauer (FEI Co.) for the high-resolution TEM images of the CS1 nanoparticles. This work is part of the research network of the Deutsche Forschungsgemeinschaft FOR1376. E.S. acknowledges PIP-CONICET 112-201001-00411 and PICT 2012-2324; whereas P.M.Q. acknowledges PICT-2014-1084 (Agencia Nacional de Promoción Científica y Tecnológica, FONCYT, préstamo BID). A grant of computing time from the Baden-Württemberg grid is gratefully acknowledged. All the data presented in this paper can be freely accessed from the Bristol's Research Data Repository (<http://data/bris.ac.uk/10.5523/bris.1om4r04s216tn164tab9nfjyfg>).

■ REFERENCES

- (1) Norskov, J. K.; Bligaard, T.; Rossmeisl, J.; Christensen, C. H. *Nat. Chem.* **2009**, *1*, 37–46.
- (2) Liu, P.; Norskov, J. K. *Phys. Chem. Chem. Phys.* **2001**, *3*, 3814–3818.

- (3) Strasser, P.; Koh, S.; Anniyev, T.; Greeley, J.; More, K.; Yu, C.; Liu, Z.; Kaya, S.; Nordlund, D.; Ogasawara, H.; Toney, M. F.; Nilsson, A. *Nat. Chem.* **2010**, *2*, 454–460.
- (4) Santos, E.; Quaino, P.; Schmickler, W. *Electrochim. Acta* **2010**, *55*, 4346–4352.
- (5) Kibler, L. A.; El-Aziz, A. M.; Hoyer, R.; Kolb, D. M. *Angew. Chem., Int. Ed.* **2005**, *44*, 2080–2084.
- (6) Bonnefont, A.; Simonov, A. N.; Pronkin, S. N.; Gerasimov, E. Y.; Pyrjaev, P. A.; Parmon, V. N.; Savinova, E. R. *Catal. Today* **2013**, *202*, 70–78.
- (7) Lee, Y. W.; Kim, N. H.; Lee, K. Y.; Kwon, K.; Kim, M.; Han, S. W. *J. Phys. Chem. C* **2008**, *112*, 6717–6722.
- (8) Quaino, P.; Santos, E.; Wolfschmidt, H.; Montero, M. A.; Stimming, U. *Catal. Today* **2011**, *177*, 55–63.
- (9) Ruvinsky, P. S.; Pronkin, S. N.; Zaikovskii, V. I.; Bernhardt, P.; Savinova, E. R. *Phys. Chem. Chem. Phys.* **2008**, *10*, 6665–6676.
- (10) Laskar, M.; Skrabalak, S. E. *J. Mater. Chem. A* **2016**, *4*, 6911–6918.
- (11) Maroun, F.; Ozanam, F.; Magnussen, O. M.; Behm, R. J. *Science* **2001**, *293*, 1811–1814.
- (12) Chen, D.; Li, C.; Liu, H.; Ye, F.; Yang, J. *Sci. Rep.* **2015**, *5*, 11949.
- (13) Wang, D.; Xin, H. L.; Wang, H.; Yu, Y.; Rus, E.; Muller, D. A.; DiSalvo, F. J.; Abruña, H. D. *Chem. Mater.* **2012**, *24*, 2274–2281.
- (14) Song, H. M.; Anjum, D. H.; Khashab, N. M. *RSC Adv.* **2012**, *2*, 3621–3624.
- (15) Song, H. M.; Anjum, D. H.; Sougrat, R.; Hedhili, M. N.; Khashab, N. M. *J. Mater. Chem.* **2012**, *22*, 25003–25010.
- (16) El-Aziz, A. M.; Kibler, L. A. *J. Electroanal. Chem.* **2002**, *534*, 107–114.
- (17) Kuo, C.-H.; Lamontagne, L. K.; Brodsky, C. N.; Chou, L.-Y.; Zhuang, J.; Sneed, B. T.; Sheehan, M. K.; Tsung, C.-K. *ChemSusChem* **2013**, *6*, 1993–2000.
- (18) Roudgar, A.; Groß, A. *Phys. Rev. B: Condens. Matter Mater. Phys.* **2003**, *67*, 033409.
- (19) Kumarakuru, H.; Cherns, D.; Oca, M. G. M. d.; Fermin, D. J. *J. Phys.: Conf. Ser.* **2012**, *371*, 012025.
- (20) Montes de Oca, M. G.; Kumarakuru, H.; Cherns, D.; Fermin, D. J. *J. Phys. Chem. C* **2011**, *115*, 10489–10496.
- (21) Montes de Oca, M. G.; Plana, D.; Celorrio, V.; Lazaro, M. J.; Fermin, D. J. *J. Phys. Chem. C* **2012**, *116*, 692–699.
- (22) Celorrio, V.; Montes de Oca, M. G.; Plana, D.; Moliner, R.; Lázaro, M. J.; Fermin, D. J. *J. Phys. Chem. C* **2012**, *116*, 6275–6282.
- (23) Plana, D.; Florez-Montano, J.; Celorrio, V.; Pastor, E.; Fermin, D. J. *Chem. Commun.* **2013**, *49*, 10962–10964.
- (24) Qin, Y.-L.; Wang, J.-W.; Wu, Y.-M.; Wang, L.-M. *RSC Adv.* **2014**, *4*, 30068–30073.
- (25) Hoshi, N.; Kida, K.; Nakamura, M.; Nakada, M.; Osada, K. *J. Phys. Chem. B* **2006**, *110*, 12480–12484.
- (26) Jiang, K.; Zhang, H.-X.; Zou, S.; Cai, W.-B. *Phys. Chem. Chem. Phys.* **2014**, *16*, 20360–20376.
- (27) Pronkin, S.; Hara, M.; Wandlowski, T. *Russ. J. Electrochem.* **2006**, *42*, 1177–1192.
- (28) Celorrio, V.; Montes de Oca, M. G.; Plana, D.; Moliner, R.; Fermin, D. J.; Lázaro, M. J. *Int. J. Hydrogen Energy* **2012**, *37*, 7152–7160.
- (29) Iwasita, T.; Nart, F. C. *Prog. Surf. Sci.* **1997**, *55*, 271–340.
- (30) Yajima, T.; Uchida, H.; Watanabe, M. *J. Phys. Chem. B* **2004**, *108*, 2654–2659.
- (31) Panayotov, D. A.; Yates, J. T., Jr. *Chem. Phys. Lett.* **2005**, *410*, 11–17.
- (32) Wolter, K.; Seiferth, O.; Kühlenbeck, H.; Bäumer, M.; Freund, H. J. *Surf. Sci.* **1998**, *399*, 190–198.
- (33) Edens, G. J.; Hamelin, A.; Weaver, M. J. *J. Phys. Chem.* **1996**, *100*, 2322–2329.
- (34) Stamenkovic, V.; Chou, K. C.; Somorjai, G. A.; Ross, P. N.; Markovic, N. M. *J. Phys. Chem. B* **2005**, *109*, 678–680.
- (35) Neurock, M.; Van Santen, R.; Koper, M. Theory and Modeling of Catalytic and Electrocatalytic Reactions. In *Catalysis and Electrocatalysis at Nanoparticle Surfaces*; Wieckowski, A., Savinova, E. R., Vayenas, C. G., Eds.; Marcel Dekker: New York, 2003; pp 1–34.
- (36) Gómez, R.; Rodes, A.; Pérez, J. M.; Feliu, J. M.; Aldaz, A. *Surf. Sci.* **1995**, *327*, 202–215.
- (37) Jiang, Y.-X.; Ding, N.; Sun, S.-G. *J. Electroanal. Chem.* **2004**, *563*, 15–21.
- (38) Álvarez, B.; Rodes, A.; Pérez, J. M.; Feliu, J. M. *J. Phys. Chem. B* **2003**, *107*, 2018–2028.
- (39) Cuesta, A.; Cabello, G.; Hartl, F. W.; Escudero-Escribano, M.; Vaz-Domínguez, C.; Kibler, L. A.; Osawa, M.; Gutiérrez, C. *Catal. Today* **2013**, *202*, 79–86.
- (40) Beltramo, G. L.; Shubina, T. E.; Koper, M. T. M. *ChemPhysChem* **2005**, *6*, 2597–2606.
- (41) Cuesta, A.; Escudero, M.; Lanova, B.; Baltruschat, H. *Langmuir* **2009**, *25*, 6500–6507.
- (42) Arenz, M.; Stamenkovic, V.; Schmidt, T. J.; Wandelt, K.; Ross, P. N.; Markovic, N. M. *Phys. Chem. Chem. Phys.* **2003**, *5*, 4242–4251.
- (43) Chen, Y.-X.; Heinen, M.; Jusys, Z.; Behm, R. *Langmuir* **2006**, *22*, 10399–10408.
- (44) Quaino, P. M.; Nazmutdinov, R.; Peiretti, L. F.; Santos, E. *Phys. Chem. Chem. Phys.* **2016**, *18*, 3659–3668.
- (45) Humphrey, J. J. L.; Plana, D.; Celorrio, V.; Sadasivan, S.; Tooze, R. P.; Rodríguez, P.; Fermín, D. J. *ChemCatChem* **2016**, *8*, 952–960.
- (46) Ignaczak, A.; Nazmutdinov, R.; Goduljan, A.; Moreira de Campos Pinto, L.; Juárez, F.; Quaino, P.; Santos, E.; Schmickler, W. *Nano Energy* **2016**, *26*, 558–564.
- (47) Arce, M. D.; Quaino, P.; Santos, E. *Catal. Today* **2013**, *202*, 120–127.
- (48) Pérez-Rodríguez, S.; Corengia, M.; García, G.; Zinola, C. F.; Lázaro, M. J.; Pastor, E. *Int. J. Hydrogen Energy* **2012**, *37*, 7141–7151.
- (49) Celorrio, V.; Calvillo, L.; Moliner, R.; Pastor, E.; Lázaro, M. J. *J. Power Sources* **2013**, *239*, 72–80.